Part I
Theory

1
Theory for Stretchable Interconnects

Jizhou Song and Shuodao Wang

1.1
Introduction

A rapidly growing range of applications demand electronic systems that cannot be formed in the conventional manner on semiconductor wafers. The most prominent example is stretchable electronics, which has a performance equal to established technologies that use rigid semiconductor wafers, but in formats that can be stretched and compressed. It enables many application possibilities such as flexible displays [1], electronic eye camera [2–4], conformable skin sensors [5], smart surgical gloves [6], and structural health monitoring devices [7]. There are primarily two directions to make stretchable electronics. One is to use intrinsically stretchable materials such as organic materials [8–13]. However, the electrical performance of organic semiconductor materials is relatively poor comparing with the well-developed, high-performance inorganic electronic materials. The other direction to achieve stretchable electronics is to use conventional semiconductors, such as silicon, and make the system stretchable. The main challenge here is to make silicon-based structures stretchable since the brittleness of silicon makes it almost impossible to be stretched. Many researches bypassed this difficulty by using stretchable interconnects [14–22].

One of the most intuitive approaches to develop stretchable interconnects is to exploit out-of-plane deflection in thin layers to accommodate strains applied in the plane. Figure 1.1 illustrates some examples of this concept. In the first case (Figure 1.1a) [17, 24, 25] of stretchable wavy ribbons, the initially flat ribbons are bonded to a prestrained elastomeric substrate. The prestrain can be induced by mechanical (or thermal) stretch along the ribbon directions. Releasing the prestrain causes a compression in the ribbon, and this compression leads to a nonlinear buckling response and results in a wavy profile. When the wavy structure is subject to stretches, the amplitudes and periods of the waves change to accommodate the deformation. In the second case (Figure 1.1b) of popup structure [26], the ribbons can be designed to bond the prestretched elastomeric substrate only at certain locations. When the prestrain is released, the ribbon on the nonbonded regions delaminates from the substrate and forms popup profile. Compared to Figure 1.1a,

Stretchable Electronics, First Edition. Edited by Takao Someya.

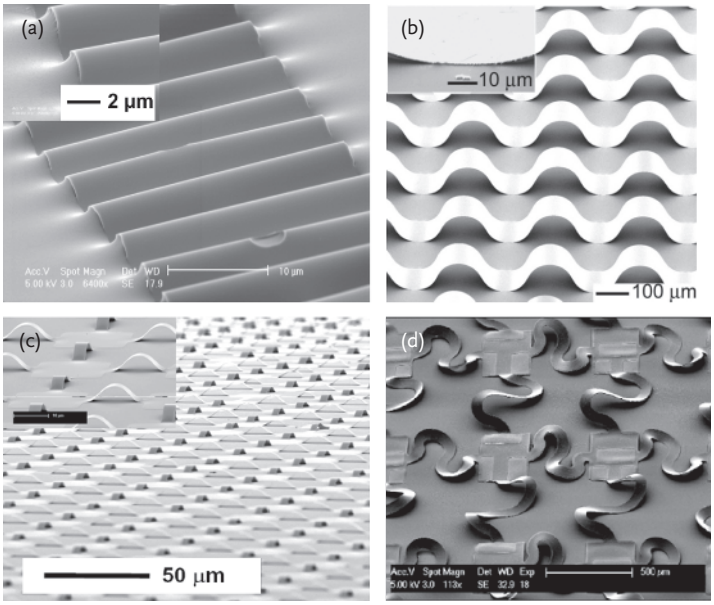

Figure 1.1 SEM images of (a) stretchable wavy ribbons, (b) popup structure, (c) noncoplanar mesh design with straight interconnects, and (d) noncoplanar mesh design with serpentine interconnects. (Reprinted with permission from Ref. [15] Copyright 2007 American Institute of Physics and Ref. [23] Copyright 2009 American Vacuum Society).

this layout has the advantage that the wavelengths can be defined precisely with a level of engineering control to have higher stretchability.

Combining the stretchable interconnects in Figure 1.1a (or Figure 1.1b) with rigid device islands, an interconnect-island structure [16, 19, 20, 22] can be developed to accommodate the deformations. Mechanical response to stretching or compression involves, primarily, deformations only in these interconnects, thereby avoiding unwanted strains in the regions of the active devices. Lacour *et al.* [16] and Kim *et al.* [19] developed a coplanar mesh design by using the wavelike interconnects, which are bonded with the substrate. Although such a coplanar mesh design can improve the stretchability to around 40%, the stretchability is still small for certain applications. Kim *et al.* [20] developed a noncoplanar mesh design (Figure 1.1c), consisting of device islands linked by popup interconnects for stretchable circuits, which can be stretched to rubber-like levels of strain (e.g., up to 100%). To further increase the stretchability, serpentine interconnects [14, 15, 19–22] can be used. Compared to the straight interconnects, the serpentine ones can accommodate larger deformation because they are much longer and can involve large twist to reduce the strains in the interconnects.

Figure 1.1d shows a SEM image of serpentine interconnects used in the noncoplanar mesh design.

For serpentine interconnects, there are no theoretical work, and many researchers have developed numerical models to study their deformations due to their complex geometries [14, 15, 19–22]. The related review is not the focus of this chapter. Here, we will review the theoretical aspects related to the designs in Figure 1.1a–c. Mechanics of stretchable wavy ribbons (Figure 1.1a) is described in Section 1.2. Analysis for small and large strains and width effect are discussed in this section. Section 1.3 describes the mechanics of popup structure (Figure 1.1b). Section 1.4 reviewed the mechanics of interconnects in the noncoplanar mesh design (Figure 1.1c). Interfacial adhesion and large deformation effect are also discussed in this section.

1.2 Mechanics of Stretchable Wavy Ribbons

The fabrication of stretchable wavy ribbons is illustrated in Figure 1.2. The flat ribbon is first chemically bonded to a prestrained compliant substrate. When the prestrain is released, the ribbon is compressed to generate the wavy layout through a nonlinear buckling response. These wavy layouts can accommodate external deformations through changes in wavelength and amplitude, which is also shown in Figure 1.2.

1.2.1 Small-Deformation Analysis

Several models [28, 29] have been developed to explain the mechanics of stretchable wavy ribbons under small deformations. For example, Huang *et al.* [29] developed an energy method to determine the buckling profile. The thin ribbon is modeled as an elastic nonlinear von Karman beam since its thickness is much smaller compared with other characteristic lengths (e.g., wavelength). The substrate is modeled as a semi-infinite solid because its thickness (~mm) is much larger than that (~μm) of film. The total energy consists of the bending energy U_b and membrane energy U_m in the thin film and strain energy U_s in the substrate.

For a stiff thin film (ribbon) with thickness h_f, Young's modulus E_f and Poisson's ratio ν_f on a prestrained compliant substrate with prestrain ε_{pre}, Young's modulus E_s, and Poisson's ratio ν_s, the wavy profile forms with the out-of-plane displacement:

$$w = A\cos(kx_1) = A\cos\left(\frac{2\pi x_1}{\lambda}\right) \tag{1.1}$$

when the prestrain is released. Here, x_1 is the coordinate along the ribbon direction, A is the amplitude, λ is the wavelength, and $k = 2\pi/\lambda$ is the wave number.

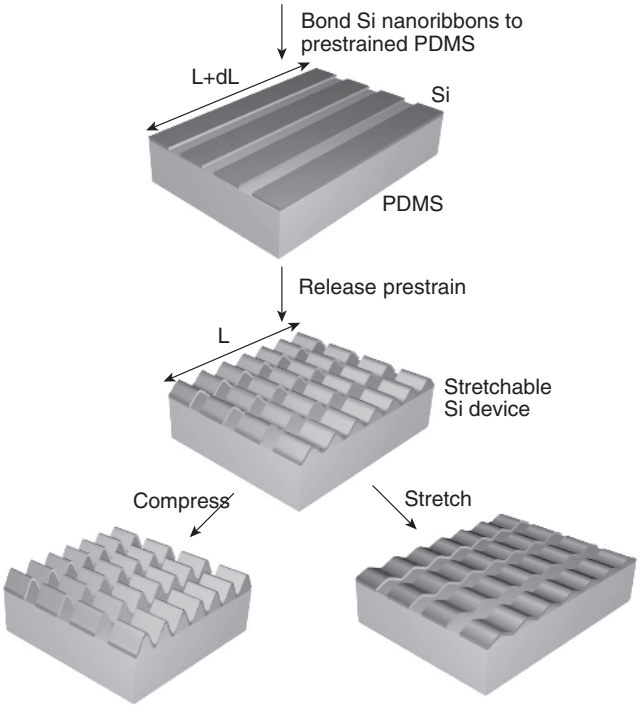

Figure 1.2 Schematic illustration of the process for fabricating buckled, or "wavy," single crystal Si ribbons on a PDMS substrate. (Reprinted with permission from Ref. [27] Copyright 2009 American Vacuum Society).

A and λ (or k) are to be determined by minimizing the total energy. The bending energy U_b can be obtained by

$$U_b = L_0 \frac{1}{\lambda} \int_0^{\lambda} \frac{\bar{E}_f h_f^3}{24} \left(\frac{d^2 w}{dx^2} \right)^2 dx = \frac{\pi^4 \bar{E}_f h_f^3 A^2}{3\lambda^4} L_0 \tag{1.2}$$

where L_0 and $\bar{E}_f = E_f / (1 - \nu_f^2)$ are the length and plane-strain modulus of the thin film, respectively.

The membrane strain ε_{11}, which determines the membrane energy in the ribbon, is related to the in-plane displacement u_1 and out-of-plane displacement w by $\varepsilon_{membrane} = du_1/dx_1 + (dw/dx_1)^2/2 - \varepsilon_{pre}$. The membrane force $N_{membrane}$ is given by $N_{membrane} = \bar{E}_f h_f \varepsilon_{membrane}$. The interfacial shear is negligible [29] and the force equilibrium equation becomes $dN_{11}/dx_1 = 0$, which gives a uniform membrane force and therefore a uniform membrane strain:

$$\varepsilon_{membrane} = \frac{\pi^2 A^2}{\lambda^2} - \varepsilon_{pre} \tag{1.3}$$

The membrane energy U_m in the film can then be obtained by

$$U_m = L_0 \frac{1}{\lambda}\int_0^{\lambda} \frac{1}{2} N_{11}\varepsilon_{11} dx = \frac{1}{2}\bar{E}_f h_f \left(\frac{\pi^2 A^2}{\lambda^2} - \varepsilon_{pre}\right)^2 L_0 \tag{1.4}$$

The strain energy in the substrate is obtained by solving a semi-infinite solid subjected to the normal displacement in Eq. (1.1) and vanishing shear on its boundary, yielding

$$U_s = \frac{\pi}{4\lambda}\bar{E}_s A^2 L_0 \tag{1.5}$$

where $\bar{E}_s = E_s/(1-\nu_s^2)$ is the plane-strain modulus of the substrate.

Energy minimization of the total energy with respect to the amplitude A and wavelength λ, that is, $\partial(U_m + U_b + U_S)/\partial A = \partial(U_m + U_b + U_S)/\partial\lambda = 0$, gives

$$\lambda_0 = 2\pi h_f \left(\frac{\bar{E}_f}{3\bar{E}_s}\right)^{1/3}, \quad A_0 = h_f\sqrt{\frac{\varepsilon_{pre}}{\varepsilon_c} - 1} \tag{1.6}$$

where

$$\varepsilon_c = \frac{1}{4}\left(\frac{3\bar{E}_s}{\bar{E}_f}\right)^{2/3} \tag{1.7}$$

is the critical strain for buckling. When $\varepsilon_{pre} < \varepsilon_c$, no buckling occurs, and the ribbon remains flat. When $\varepsilon_{pre} > \varepsilon_c$, the ribbon buckles such that the membrane strain remains a constant $\varepsilon_{membrane} = -\varepsilon_c$. The (maximum) bending strain is equal to the maximum curvature times the half thickness $h_f/2$, that is, $\varepsilon_{bending} = \frac{2\pi^2}{\lambda^2} A h_f$. The peak strain ε_{peak} in the film is the summation of membrane and bending strains. In most cases of practical interest, the bending strain is much larger than the membrane strain. For example, the membrane strain is only 0.034% for the Si ribbon ($E_f = 130\,\text{GPa}$, $\nu_f = 0.27$) on PDMS substrate ($E_s = 1.8\,\text{MPa}$, $\nu_s = 0.48$). Therefore, the peak strain can be approximated by

$$\varepsilon_{peak} \approx \varepsilon_{bending} = 2\sqrt{\varepsilon_{pre}\varepsilon_c} \tag{1.8}$$

Because the magnitude of critical strain is very small, the magnitude of the peak strain ε_{peak} is much smaller than the prestrain ε_{pre}. For example, ε_{peak} is only 1.8% for the Si/PDMS system when $\varepsilon_{pre} = 23.8\%$. This provides an effective level of stretchability/compressibility of the system.

For the buckled system subjected to the applied strain $\varepsilon_{applied}$, the above results can be obtained by simply replacing the prestrain ε_{pre} by $\varepsilon_{pre} - \varepsilon_{applied}$. The wavelength and amplitude become

$$\lambda = 2\pi h_f \left(\frac{\bar{E}_f}{3\bar{E}_s}\right)^{1/3}, \quad A = h_f\sqrt{\frac{\varepsilon_{pre} - \varepsilon_{applied}}{\varepsilon_c} - 1} \tag{1.9}$$

and the peak strain in the ribbon is

$$\varepsilon_{\text{peak}} \approx 2\sqrt{(\varepsilon_{\text{pre}} - \varepsilon_{\text{applied}})\varepsilon_{\text{c}}} \tag{1.10}$$

1.2.2 Finite-Deformation Analysis

The wavelengths in Eqs. (1.6) and (1.9) are constant and strain-independent, and have been widely used in high precision micro and nano-metrology methods [30, 31]. However, when the prestrain is large, the experiments [32–34] showed that the wavelength decreases with increasing prestrain. Figure 1.3 clearly shows this dependence for the Si/PDMS system. Jiang *et al.* [34] and Song *et al.* [35] pointed out that the strain-dependent wavelength is due to the finite deformation (i.e., large strain) in the compliant substrate and established a buckling theory that accounts for finite geometry change (i.e., different strain-free or stress-free states for the ribbon and substrate) as shown in Figure 1.4, nonlinear strain-displacement relation and nonlinear constitutive model for the substrate to explain this finite deformation effect.

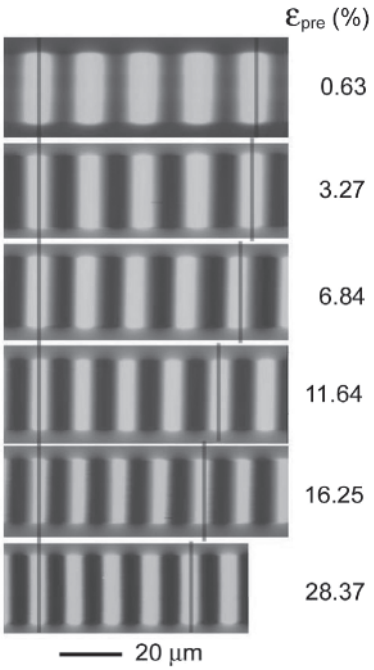

Figure 1.3 Stacked plane-view AFM images of buckled Si ribbons (100 nm thick) on PDMS for different levels of prestrain. (Reprinted with permission from Ref. [35] Copyright 2008 Elsevier Ltd).

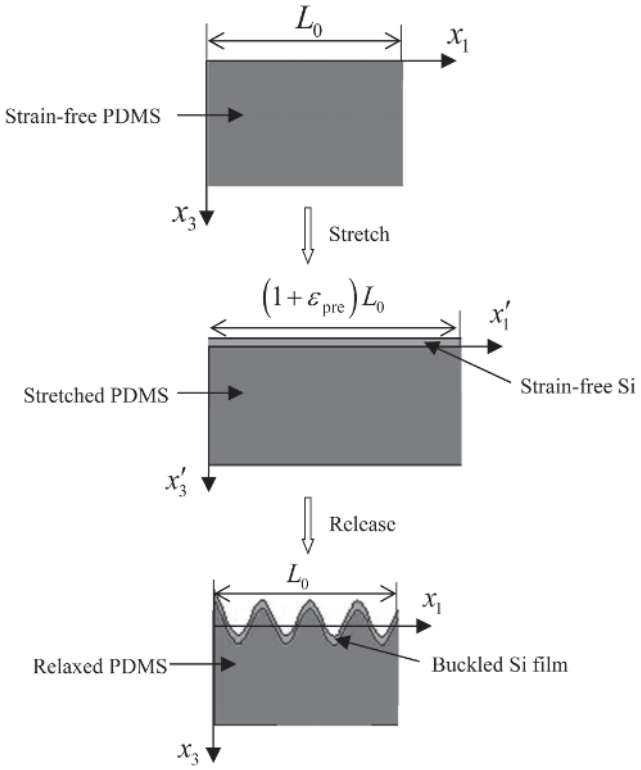

Figure 1.4 Three sequential configurations for the thin film/substrate buckling process. The top figure shows the undeformed substrate with the original length L_0, which represents the zero strain energy state. The middle figure shows the substrate deformed by the prestrain and the integrated film, which represents zero strain energy state for the thin film. The bottom figure shows the deformed (buckled) configuration. (Reprinted with permission from Ref. [35] Copyright 2008 Elsevier Ltd).

The out-of-plane displacement of the buckled thin ribbon can be represented by

$$w = A\cos\left(\frac{2\pi x_1}{\lambda}\right) = A\cos\left[\frac{2\pi x_1'}{(1+\varepsilon_{pre})\lambda}\right] \tag{1.11}$$

in the strain-free configuration (middle figure, Figure 1.4) as well as in the relaxed configuration (bottom figure, Figure 1.4). The coordinate x_1' in the middle figure is related to x_1 in the bottom figure by $x_1' = (1+\varepsilon_{pre})x_1$.

The thin ribbon is still modeled as a von Karman beam. Using similar approach in Section 1.2.1, the bending energy and membrane energy in the film can be obtained as

$$U_{\mathrm{b}} = \frac{\pi^4}{3}\frac{\bar{E}_{\mathrm{f}} h_{\mathrm{f}}^3 A^2}{\left[\left(1+\varepsilon_{\mathrm{pre}}\right)\lambda\right]^4}\left(1+\varepsilon_{\mathrm{pre}}\right)L_0 \tag{1.12}$$

and

$$U_{\mathrm{m}} = \frac{1}{2}\bar{E}_{\mathrm{f}} h_{\mathrm{f}}\left[\frac{\pi^2 A^2}{\left(1+\varepsilon_{\mathrm{pre}}\right)^2\lambda^2} - \frac{\varepsilon_{\mathrm{pre}}}{1+\varepsilon_{\mathrm{pre}}}\right]^2\left(1+\varepsilon_{\mathrm{pre}}\right)L_0 \tag{1.13}$$

respectively, where $(1 + \varepsilon_{\mathrm{pre}})L_0$ is the initial length of strain-free Si thin ribbon (middle figure, Figure 1.4).

The geometric and material nonlinearity are considered in the modeling of substrate. All the governing equations are in terms of the coordinates for the strain-free configuration of PDMS substrate (i.e., x_1 and x_3 in Figure 1.4). The Green strains E_{IJ} in the substrate are related to the displacements $u_1(x_1,x_3)$ and $u_3(x_1,x_3)$ by

$$E_{IJ} = \frac{1}{2}\left(\frac{\partial u_I}{\partial x_J} + \frac{\partial u_J}{\partial x_I} + \frac{\partial u_K}{\partial x_I}\frac{\partial u_K}{\partial x_J}\right) \tag{1.14}$$

where the subscripts I and J are 1 or 3. To account for the material nonlinearity, the Neo–Hookean constitutive law is used to represent the substrate

$$T_{IJ} = \frac{\partial W_{\mathrm{s}}}{\partial E_{IJ}} \tag{1.15}$$

where T_{IJ} is the second Piola–Kirchhoff stress, and the strain energy density W_{s} takes the form $W_{\mathrm{s}} = \frac{E_{\mathrm{s}}}{6(1-2\nu_{\mathrm{s}})}(J-1)^2 + \frac{E_{\mathrm{s}}}{4(1+\nu_{\mathrm{s}})}(\bar{I}_1 - 3)$. Here J is the volume change at a point and is the determinant of deformation gradient F_{ij}, $\bar{I}_1$ is the trace of the left Cauchy–Green strain tensor $B_{IJ} = F_{Ik}F_{Jk}$ times $J^{-2/3}$. The force equilibrium equation for finite deformation is

$$\left(F_{iK}T_{JK}\right)_{,J} = 0 \tag{1.16}$$

The perturbation method is used to find the solutions for the substrate, and the strain energy is obtained by Song *et al.* [35] as

$$U_{\mathrm{s}} = \frac{\pi}{3}\frac{E_{\mathrm{s}}A^2}{\lambda}\left(1 + \frac{5}{32}\frac{\pi^2 A^2}{\lambda^2}\right)L_0 \tag{1.17}$$

where L_0 is the original length of the substrate.

Minimization of the total energy gives the wavelength and amplitude

$$\lambda = \frac{\lambda_0}{\left(1+\varepsilon_{\mathrm{pre}}\right)\left(1+\xi\right)^{1/3}}, \quad A \approx \frac{A_0}{\sqrt{1+\varepsilon_{\mathrm{pre}}}\left(1+\xi\right)^{1/3}} \tag{1.18}$$

where λ_0 and A_0 are, respectively, the wavelength and amplitude in Eq. (1.6) from small-deformation analysis, and $\xi = 5\varepsilon_{\mathrm{pre}}(1 + \varepsilon_{\mathrm{pre}})/32$. Contrary to the small-

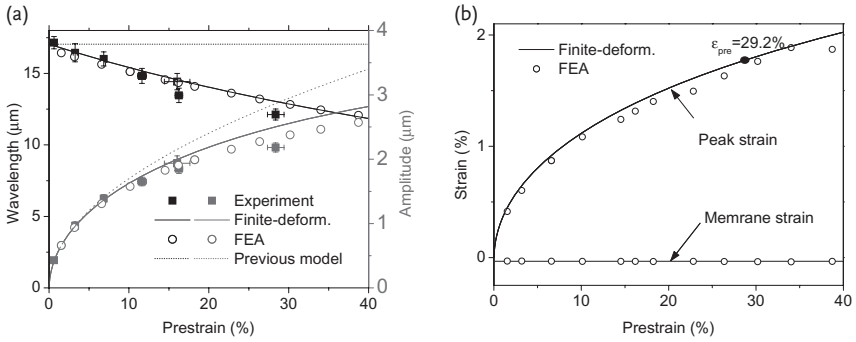

Figure 1.5 (a) Wavelength and amplitude (b) membrane and peak strains of buckled Si ribbons (100 nm thick) on PDMS as functions of the prestrain. (Reprinted with permission from Ref. [35] Copyright 2008 Elsevier Ltd).

deformation theory, the wavelength decreases with ε_{pre}, but the amplitude increases with ε_{pre}. Both wavelength and amplitude agree well with experimental data and finite element simulations without any parameter fitting as shown in Figure 1.5a.

The membrane and bending strain can be obtained as

$$\varepsilon_{membrane} = -\frac{1+\frac{\xi}{3}}{(1+\xi)^{1/3}}\varepsilon_c,\ \varepsilon_{bending} = 2(1+\xi)^{1/3}\sqrt{\varepsilon_c}\sqrt{\frac{\varepsilon_{pre}}{1+\varepsilon_{pre}} - \frac{1+\frac{\xi}{3}}{(1+\xi)^{1/3}}\varepsilon_c} \tag{1.19}$$

For large prestrain, the peak strain, which is summation of $\varepsilon_{membrane}$ and $\varepsilon_{bending}$, is given by

$$\varepsilon_{peak} \approx 2\sqrt{\varepsilon_{pre}\varepsilon_c}\frac{(1+\xi)^{1/3}}{\sqrt{1+\varepsilon_{pre}}} \tag{1.20}$$

Figure 1.5b shows ε_{peak} and $\varepsilon_{membrane}$ as a function of ε_{pre}. Both the membrane and peak strains agree well with finite element analysis. Compared to the peak strain, the membrane strain is much smaller and negligible. Compared to the prestrain, the peak strain is much smaller, and therefore the system can provide an effective level of stretchability/compressibility. For example, for $\varepsilon_{fracture}$ = 1.8%, the maximum allowable prestrain is obtained as ~ 29% by $\varepsilon_{peak} = \varepsilon_{fracture}$, which is almost 20 times larger than $\varepsilon_{fracture}$.

For the buckled system subjected to the applied strain $\varepsilon_{applied}$, Song *et al.* [35] obtained the total energy of the system using the perturbation method and gave the wavelength and amplitude

$$\lambda'' = \frac{\lambda_0(1+\varepsilon_{applied})}{(1+\varepsilon_{pre})(1+\varepsilon_{applied}+\zeta)^{1/3}},\quad A'' \approx h_f\frac{\sqrt{(\varepsilon_{pre}-\varepsilon_{applied})/\varepsilon_c - 1}}{\sqrt{1+\varepsilon_{pre}}(1+\varepsilon_{applied}+\zeta)^{1/3}} \tag{1.21}$$

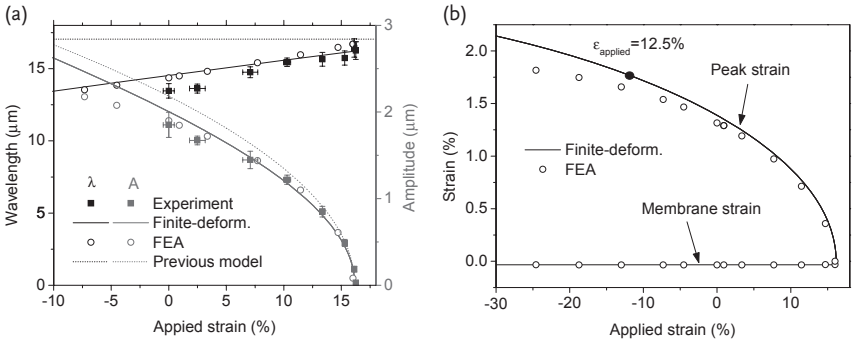

Figure 1.6 (a) Wavelength and amplitude (b) membrane and peak strains of buckled Si ribbons (100 nm thick) on PDMS formed with a prestrain of 16.2% as a function of the applied strain. (Reprinted with permission from Ref. [35] Copyright 2008 Elsevier Ltd).

where $\xi = 5(\varepsilon_{pre} - \varepsilon_{applied})(1 + \varepsilon_{pre})/32$. Figure 1.6a shows the wavelength and amplitude as a function of applied strain for a buckled Si/PDMS system formed at the prestrain 16.2%. Both amplitude and wavelength agree well with experimental data and finite element simulations. As the tensile strain increases, the wavelength increases, but the amplitude decreases. Once the tensile strain reaches the prestrain plus the critical strain, the amplitude becomes zero and further stretch of $\varepsilon_{fracture}$ will fracture the film. Therefore, the stretchability is given by $\varepsilon_{pre} + \varepsilon_{fracture} + \varepsilon_c$. The membrane and peak strains in the ribbon are obtained as

$$\varepsilon_{membrane} = -\frac{(1+\zeta/3)}{(1+\zeta)^{1/3}}\varepsilon_c, \quad \varepsilon_{peak} \approx 2\sqrt{(\varepsilon_{pre} - \varepsilon_{applied})\varepsilon_c}\,\frac{(1+\varepsilon_{applied}+\zeta)^{1/3}}{\sqrt{1+\varepsilon_{pre}}} \tag{1.22}$$

Figure 1.6b shows ε_{peak} and $\varepsilon_{membrane}$ as functions of $\varepsilon_{applied}$ under the prestrain 16.2%. The analytical solutions agree well with finite element simulations.

The compressibility is the maximum applied compressive strain when the peak Si strain reaches $\varepsilon_{fracture}$, and it is well approximated by $\frac{\varepsilon_{fracture}^2}{4\varepsilon_c}\left(1+\frac{43}{48}\frac{\varepsilon_{fracture}^2}{4\varepsilon_c}\right) - \varepsilon_{pre}$. Figure 1.7 shows the stretchability and compressibility versus the prestrain. The stretchability increases with increasing the prestrain, while the compressibility decreases. When the prestrain is 13.4%, the stetchability and compressibility is equal.

1.2.3 Ribbon Width Effect

The analyses in the above sections assumed that the thin ribbon width is much larger than the wavelength such that the deformation is plane strain. However, this assumption may not hold for small-width ribbons. Figure 1.8 shows the

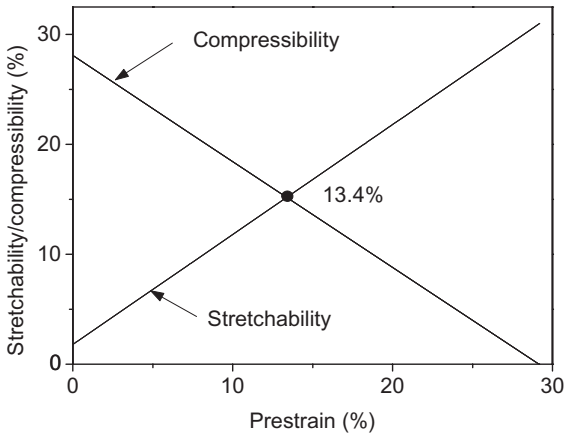

Figure 1.7 Strechability and compressibility of buckled Si ribbons (100 nm thickness) on PDMS. (Reprinted with permission from Ref. [35] Copyright 2008 Elsevier Ltd).

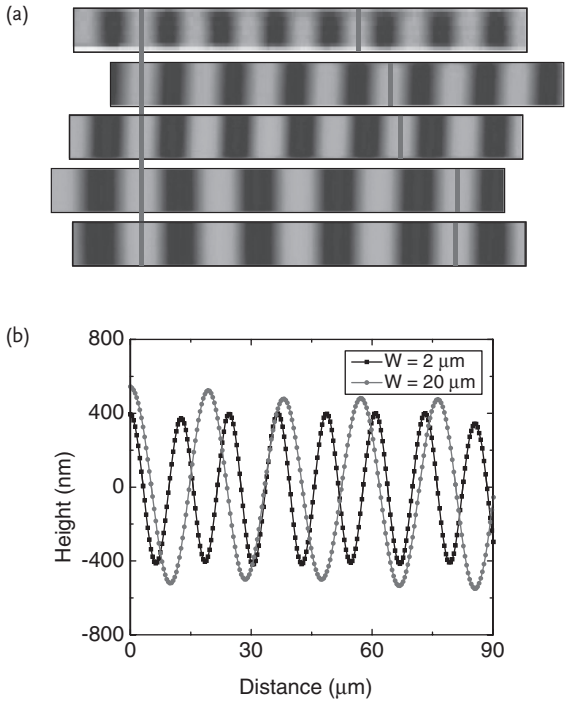

Figure 1.8 (a) Stacked plane-view AFM images of buckled Si ribbons for different widths of 2, 5, 20, 50, and 100 μm (from top to bottom). (b) AFM line-cut profiles along the buckled wavy Si ribbons for 2 and 20 μm wide ribbons. (Reprinted with permission from Ref. [17] Copyright 2008 Elsevier Ltd).

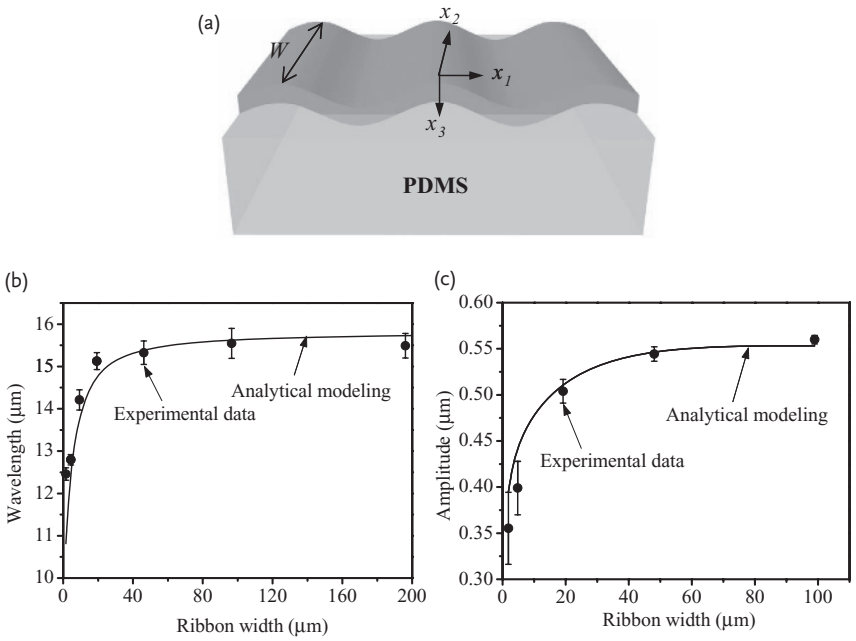

Figure 1.9 (a) Schematic illustration of the geometry and coordinate system for a buckled single thin film on PDMS substrate. W is the width of the thin film. (b) Wavelength and (c) amplitude of the buckling profile as functions of the width of silicon thin films. The theoretical analysis is shown in solid line, and the experimental data is shown in filled circles. (Reprinted with permission from Ref. [17] Copyright 2008 Elsevier Ltd).

strong effect of ribbon width effect for the Si/PDMS system. Figure 1.8a shows the plane-view (from top to bottom) AFM images of Si ribbons for different widths 2, 5, 20, 50, and 100 μm. It clearly shows that the wavelength increases with the increase of the ribbon width and approaches to a constant at a finite value. The linecut profiles from AFM measurements in Figure 1.8b for the 2 and 20 μm wide ribbons also shows this strong ribbon width effect

Jiang *et al.* [27] studied the ribbon width effect on the buckling profile. The ribbon width is denoted by W as shown in Figure 1.9a. Similar to Section 1.2.1, the total energy of the system consists of membrane and bending energy in the film and strain energy in the substrate. The membrane energy and bending energy in Eqs. (1.2) and (1.4) still hold except that they need to be multiplied by the ribbon width W. The substrate is modeled as a three-dimensional, semi-infinite solid with traction-free surface except for the portion underneath the ribbon. The strain energy in the substrate can be obtained analytically as

$$U_s = \frac{1}{\pi \bar{E}_s}\left[E_f k h_f A\left(\frac{1}{12}k^2 h_f^2 + \frac{1}{4}A^2 k^2 - \varepsilon_{pre}\right)\right]^2 \rho(Wk) \tag{1.23}$$

where

$$\rho(x) = -1 + xY_1(x) + x^2Y_0(x) + \frac{\pi}{2}x^2\left[H_1(x)Y_0(x) + H_0(x)Y_1(x)\right] \tag{1.24}$$

is a nondimensional function, Y_n ($n = 0,1,2, \ldots$) is the Bessel function of the second kind, and H_n ($n = 0,1,2, \ldots$) denotes the Struve function.

The energy minimization gives the following governing equation for the wave number k:

$$\frac{\bar{E}_s W^3}{E_f h_f^3} = \frac{2}{3\pi}\frac{W^2k^2\left[\rho(Wk)\right]^2}{\rho(Wk) + 1 - WkY_1(Wk)} \tag{1.25}$$

From Eq. (1.25), we have

$$k = \frac{1}{h_f}\left(\frac{3\bar{E}_s}{E_f}\right)^{1/3} f\left[\left(\frac{\bar{E}_s}{E_f}\right)^{1/3}\frac{W}{h_f}\right] \tag{1.26}$$

where f is a nondimensional function be determined numerically by Eq. (1.25), which can be well approximated by the simple relation $f(x) \approx \coth\left(\frac{16}{15}x^{1/4}\right)$. Therefore, the wavelength $\lambda = 2\pi/k$ is given by

$$\lambda = 2\pi h_f\left(\frac{E_f}{3\bar{E}_s}\right)^{1/3}\tanh\left\{\frac{16}{15}\left[\left(\frac{\bar{E}_s}{E_f}\right)^{1/3}\frac{W}{h_f}\right]^{1/4}\right\} \tag{1.27}$$

The energy minimization gives the amplitude as

$$A = \begin{cases} \dfrac{2}{k}\sqrt{\varepsilon_{pre} - F} & \varepsilon_{pre} \geq F \\ 0 & \varepsilon_{pre} < F \end{cases} \tag{1.28}$$

where $F = \dfrac{\pi W\bar{E}_s}{4hE_f\rho(Wk)} + \dfrac{1}{12}h_f^2k^2$. Figure 1.9b and c shows the buckling wavelength and amplitude versus the ribbon width for 100 nm thick Si ribbon under the pre-strain 1.3%, respectively. The solid lines are the analytical solutions from Eqs. (1.27) and (1.28), and the experimental results are plotted by filled circles. Both wavelength and amplitude agree well with experiments. The width effect is negligible for wide ribbons (i.e., >50 μm). However, when the ribbon is narrow, the width effect is strong and cannot be ignored. For example, for 2 μm-wide ribbon, the buckling wavelength is 12.5 μm, and it will increase by 25% to 15.5 μm for 100 μm-wide ribbon.

1.3 Mechanics of Popup Structure

Figure 1.10 schematically illustrates the fabrication of popup structure on compliant substrates [23, 26], which combines lithographically patterned surface bonding

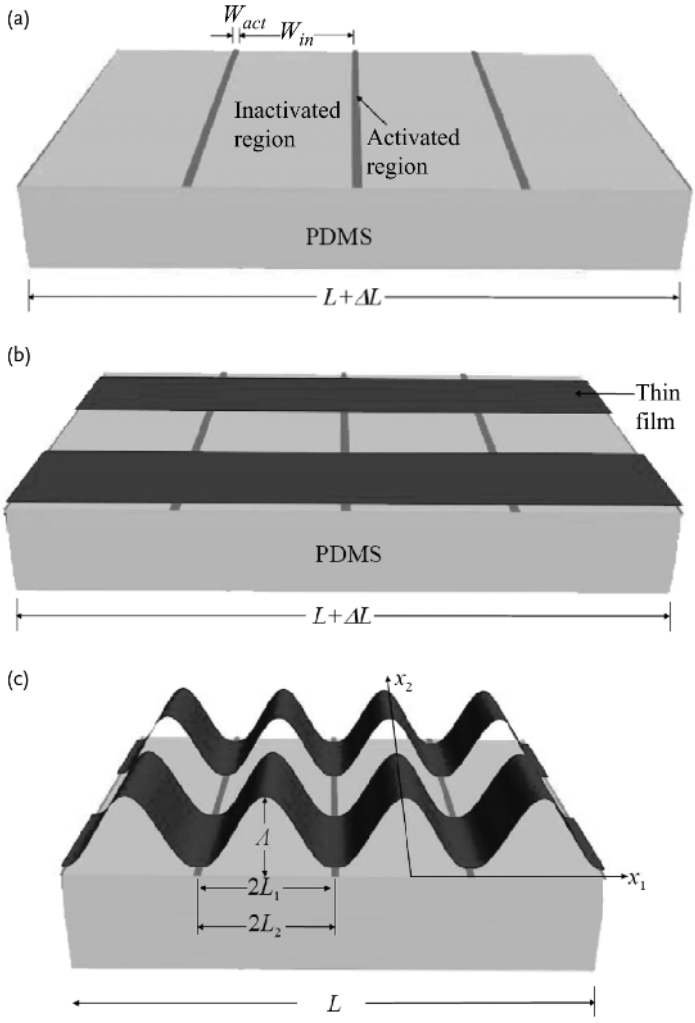

Figure 1.10 Processing steps for precisely controlled thin film buckling on elastomeric substrate. (a) Prestrained PDMS with periodic activated and inactivated patterns. L is the original length of PDMS, and ΔL is the extension. The widths of activated and inactivated sites are denoted as W_{act} and W_{in}, respectively. (b) A thin film parallel to the prestrain direction is attached to the prestrained and patterned PDMS substrate. (c) The relaxation of the prestrain ε_{pre} in PDMS leads to buckles of thin film. The wavelength of the buckled film is $2L_1$, and the amplitude is A. $2L_2$ is the sum of activated and inactivated regions after relaxation. (Reprinted with permission from Ref. [15] Copyright 2007 American Institute of Physics).

chemistry and a buckling process. The ribbon is bonded to the prestrained substrate only at certain locations. Let W_{act} denote the width of activated regions, where chemical bonding occurs between the ribbon and the substrate, and W_{in} denote the width of inactivated regions, where only weak van der Waals interactions occur at the interface as shown in Figure 1.10a. Thin ribbons are then attached to the prestrained and patterned PDMS substrate (Figure 1.10b) with the ribbon direction parallel to the prestreched direction. Releasing the prestrain leads to compression, which causes the ribbon on the inactivated regions to buckle and form the popup structure as shown in Figure 1.10c.

Jiang *et al.* [23] developed an analytical model to study the buckling behavior of such systems and to predict the maximum strain in the ribbons as a function of interfacial pattern. The buckling profile of the ribbon can be expressed as

$$w = \begin{cases} w_1 = \dfrac{1}{2} A\left(1 + \cos\dfrac{\pi x_1}{L_1}\right), & -L_1 < x_1 < L_1 \\ w_2 = 0, & L_1 < |x_1| < L_2 \end{cases} \tag{1.29}$$

where A is the buckling amplitude to be determined, $2L_1 = \dfrac{W_{in}}{1+\varepsilon_{pre}}$ is the buckling wavelength, and $2L_2 = \dfrac{W_{in}}{1+\varepsilon_{pre}} + W_{act}$ is the sum of activated and inactivated regions after relaxation (Figure 1.10c). The bending and membrane energy in the thin film can be obtained as

$$U_{bending} = \int_{-L_2}^{L_2} \frac{1}{2} \frac{\bar{E}_f h_f^3}{12} \left(\frac{d^2 w}{dx_1^2}\right)^2 dx_1 = \frac{\pi^4}{96} \frac{\bar{E}_f h_f^3 A^2}{L_1^3} \tag{1.30}$$

and

$$U_{membrane} = \bar{E}_f h_f \left(\frac{\pi^2 A^2}{16 L_1 L_2} - \varepsilon_{pre}\right)^2 L_2 \tag{1.31}$$

respectively. It should be noticed that the substrate energy

$$U_{substrate} = 0 \tag{1.32}$$

because the substrate has zero displacement at the interface where it remains intact and vanishing stress traction at the long and buckled portion.

Energy minimization of the total energy gives the amplitude as

$$A = \frac{4}{\pi} \sqrt{L_1 L_2 \left(\varepsilon_{pre} - \varepsilon_c\right)} \tag{1.33}$$

where $\varepsilon_c = h_f^2 \pi^2 / \left(12 L_1^2\right)$ is the critical strain for buckling, which is identical to the Euler buckling strain for a doubly clamped beam with length $2L_1$. The critical strain ε_c is usually a small number in most practical applications. For example, ε_c is on the order of 10^{-6} for a typical wavelength $2L_1 \sim 200\,\mu m$ and ribbon thickness

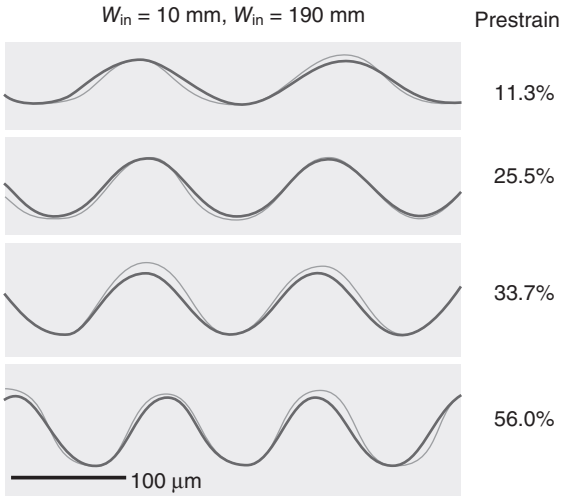

Figure 1.11 Buckled GaAs thin films on patterned PDMS substrate with $W_{in} = 10\,\mu m$ and $W_{in} = 190\,\mu m$ for different prestrain levels, 11.3%, 25.5%, 33.7%, and 56.0% (from top to bottom). The bold lines are the profiles of the buckled GaAs thin film predicted by the analytical solution. (Reprinted with permission from Ref. [15] Copyright 2007 American Institute of Physics).

$h_f \sim 0.1\,\mu m$. Therefore, the buckling amplitude A in Eq. (1.33) can be approximately by

$$A \approx \frac{4}{\pi}\sqrt{L_1 L_2 \varepsilon_{pre}} = \frac{2}{\pi}\frac{\sqrt{W_{in}(W_{in}+W_{act})\varepsilon_{pre}}}{1+\varepsilon_{pre}} \tag{1.34}$$

which is completely determined by the interfacial patterns (W_{in} and W_{act}) and the prestrain. The comparison of buckled profiles from analytical prediction (dot lines) and experiments is shown in Figure 1.11 for the case of $W_{act} = 10\,\mu m$ and $W_{in} = 190\,\mu m$. Both wavelength and amplitude agree well with experiments.

The maximum strain in the ribbon can be approximately by the bending strain since the membrane strain is negligible (~10^{-6}). The bending strain is equal to the maximum curvature times the half thickness and therefore, we have

$$\varepsilon_{peak} = \frac{h_f}{2}\max\left(\frac{d^2 w}{dx_1^2}\right) = \frac{h_f \pi}{L_1^2}\sqrt{L_1 L_2 \varepsilon_{pre}} \tag{1.35}$$

The maximum strain is much smaller than the prestrain. For example, for $h_f = 0.3\,\mu m$, $W_{act} = 10\,\mu m$, $W_{in} = 400\,\mu m$, and $\varepsilon_{pre} = 60\%$, ε_{peak} is only 0.6%, which is two orders of magnitude smaller than the 60% prestrain. For much smaller active region (i.e., $W_{act} \ll W_{in}$), the maximum strain in Eq. (1.35) can be approximated by $\varepsilon_{peak} \approx \pi h_f \sqrt{\varepsilon_{pre}} / L_1$.

1.4
Mechanics of Interconnects in the Noncoplanar Mesh Design

Figure 1.12 schematically illustrates the fabrication of a noncoplanar mesh design consisting of stretchable interconnects and device islands [20]. The device islands are chemically bonded to a prestrained substrate, while the interconnects are loosely bonded. When the prestrain in the substrate is released, the interconnects buckle out of the surface and form arc-shaped structures. Due to the low adhesion, narrow geometries, and low stiffness of interconnects, the deformation localizes only to the interconnects and therefore the device islands experience small strains. Figure 1.13 shows the initial, strain-free configuration X of the interconnects and the buckled configuration x, respectively. The initial distance between the ends of interconnect is L_0, and changes to $L = L_0/(1 + \varepsilon_{pre})$ after the prestrain is released.

1.4.1
Global Buckling of Interconnects

Song *et al.* [36] established a mechanics model to understand the buckling behavior of the interconnects. Compared with the model in Section 1.3, the geometry

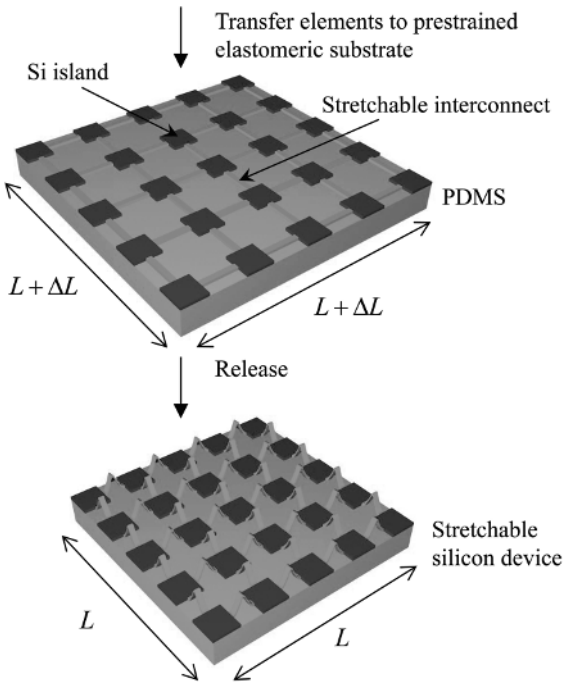

Figure 1.12 A schematic illustration of the process for fabricating noncoplanar mesh designs on a complaint substrate. (Reprinted with permission from Ref. [23] Copyright 2009 American Institute of Physics).

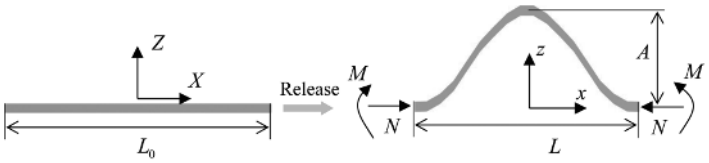

Figure 1.13 Schematic diagram of mechanics model for the interconnect region of a noncoplanar mesh structure. (Reprinted with permission from Ref. [23] Copyright 2009 American Institute of Physics).

change is accounted here. The out-of-plane displacement, w, of the interconnect takes the form

$$w = \frac{A}{2}\left(1+\cos\frac{2\pi x}{L}\right) = \frac{A}{2}\left(1+\cos\frac{2\pi X}{L_0}\right) \tag{1.36}$$

which satisfies vanishing displacement and slope at the two ends $X = \pm L_0/2$, and the amplitude A is to be determined by energy minimization. The bending energy and membrane energy can be obtained as

$$U_{\text{bending}} = \frac{\pi^4 E h^3 A^2}{12 L_0^3} \tag{1.37}$$

and

$$U_{\text{membrane}} = \frac{1}{2} E h L_0 \left(\frac{\pi^2 A^2}{4 L_0^2} - \varepsilon\right)^2 \tag{1.38}$$

where $\varepsilon = (L_0 - L)/L_0$ is the compressive strain, E and h are the Young's modulus and thickness of the interconnects, respectively. Minimization of total energy $U_{\text{global}} = U_{\text{membrane}} + U_{\text{bending}}$ in the interconnect gives the amplitude

$$A = \frac{2L_0}{\pi}\sqrt{\varepsilon - \varepsilon_c} \tag{1.39}$$

where $\varepsilon_c = \pi h^2/3L_0^2$ is the critical buckling strain for Euler buckling of a doubly clamped beam. The maximum (compressive) strain in the interconnect is the sum of bending (curvature * $h/2$) and membrane strains ($-\varepsilon_c$). Because the membrane strain is very small compared to the bending strain, the peak strain in the interconnects is given by

$$\varepsilon_{\text{peak}} \approx \frac{2\pi h}{L_0}\sqrt{\varepsilon} \tag{1.40}$$

In experiments, the initial interconnect length is $L_0 = 20\,\mu\text{m}$ and after relaxation, the length becomes $L = 17.5\,\mu\text{m}$, which corresponds to a compressive strain $\varepsilon = 12.5\%$. The thickness of interconnects is $h = 50\,\text{nm}$. The critical buckling strain is $\varepsilon_c = 0.0021\%$. The predicted amplitude by Eq. (1.39) is $4.50\,\mu\text{m}$, which

agrees well with the experimental value 4.76 μm. Equation (1.40) shows that thin and long interconnects give small maximum strain because it is proportional to the ratio of the interconnect thickness to the length, h/L_0, which provides a design rule for the buckled interconnects.

1.4.2 Adhesion Effect on Buckling of Interconnects

It should be noticed that other buckling modes may occur if the prestrain is small. Figure 1.14 shows the top and cross-sectional views of a linear array of interconnected silicon islands on a PDMS substrate subjected to low, medium, and high levels of compressive strains. When the compressive strain is small, the interconnect remains flat, and there is no buckling. With the increase of the compressive strain, local buckling (i.e., small multiple waves) may occur. Further increasing the compressive strain up to 8.5%, local buckling transforms to global buckling as the small multiple waves merge together.

Ko *et al.* [37] and Wang *et al.* [38] developed a mechanics model to explain the occurrence of different buckling modes by accounting for the adhesion between the interconnect and substrate. Prior to buckling, the interconnect remains flat and the total energy is

$$U_{\text{flat}} = \frac{1}{2} EhL_0\varepsilon^2 - \gamma L_0 \tag{1.41}$$

where γ is the work of adhesion between the interconnect and substrate, the first term is the membrane energy $U_{\text{membrane}} = EhL_0\varepsilon^2/2$ and the second is the adhesion

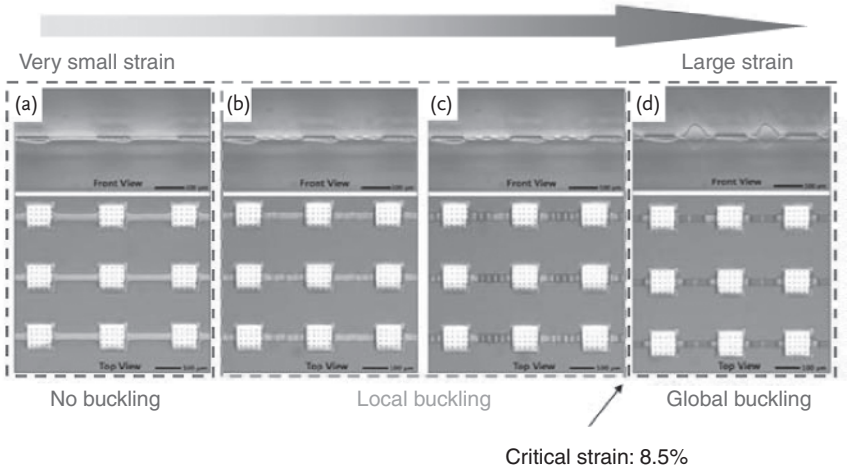

Figure 1.14 Cross-sectional and top views of a linear array of interconnected silicon islands on a PDMS substrate subjected to low, medium, and high levels of compressive strains. (Reprinted with permission from Ref. [22] Copyright 2009 John Wiley and Sons).

energy. For global buckling, the summation of Eqs. (1.37) and (1.38) gives the total energy as

$$U_{\text{global}} = EhL\varepsilon_{\text{c}}\left(\varepsilon - \frac{\varepsilon_{\text{c}}}{2}\right) \tag{1.42}$$

where $\varepsilon_{\text{c}} = \pi h^2/3l_0^2$. The critical strain for the transition from flat to global buckling can be obtained by $U_{\text{flat}} = U_{\text{global}}$ as

$$\left(\frac{\varepsilon}{\varepsilon_{\text{c}}}\right)_{\text{flat-global}} = 1 + \sqrt{\frac{2\gamma}{Eh\varepsilon_{\text{c}}^2}} \tag{1.43}$$

For local buckling, the interconnect buckles to form small multiple waves with amplitude a and wavelength l to be determined. The membrane energy is obtained as $U_{\text{membrane}} = \frac{1}{2}EhL\left(\frac{\pi^2 a^2}{4lL_0} - \varepsilon\right)^2$, the bending energy $U_{\text{bending}} = \frac{\pi^4 Eh^3 a^2}{12l^3}$, and adhesion energy $U_{\text{adhesion}} = -\gamma(L_0 - l)$. Energy minimization gives the amplitude $a = \frac{2l}{\pi}\sqrt{\left(\varepsilon - \frac{\pi^2 h^2}{3l^2}\right)\frac{L_0}{l}}$ and the governing equation for l as

$$\frac{\pi^2 h^3}{3l^3}\left(\frac{\pi^2 h^2}{3l^2} - \varepsilon\right) + \frac{\gamma}{2EL_0} = 0 \tag{1.44}$$

Therefore, we have $l = g\left(\varepsilon, \frac{\gamma}{EL_0}\right)h$, where g is a nondimensional function to be determined numerically by Eq. (1.44). The total energy for local buckling is then obtained as

$$U_{\text{local}} = \frac{\pi^2 EhL}{3g^2\left(\varepsilon, \frac{\gamma}{EL}\right)}\left[\varepsilon - \frac{\pi^2}{6g^2\left(\varepsilon, \frac{\gamma}{EL}\right)}\right] - \gamma L\left[1 - \frac{h}{L}g\left(\varepsilon, \frac{\gamma}{EL}\right)\right] \tag{1.45}$$

The critical strain for the transition from flat to local buckling can be obtained by $U_{\text{flat}} = U_{\text{local}}$ as

$$\left(\frac{\varepsilon}{\varepsilon_c}\right)_{\text{flat-local}} = 5\left(\frac{\gamma}{8Eh\varepsilon_{\text{c}}^2}\right)^{2/5} \tag{1.46}$$

Equations (1.43) and (1.46) give a simple criterion to predict buckling patterns. When the critical strain in Eq. (1.46) is larger than that in Eq. (1.43), that is, $\frac{\gamma}{8Eh\varepsilon_{\text{c}}^2} \le 1$, global buckling occurs, and there is no local buckling. When the critical strain in Eq. (1.46) is smaller than that in Eq. (1.43), that is, $\frac{\gamma}{8Eh\varepsilon_{\text{c}}^2} > 1$, local buckling occurs first and as the compressive strain increases; global buckling

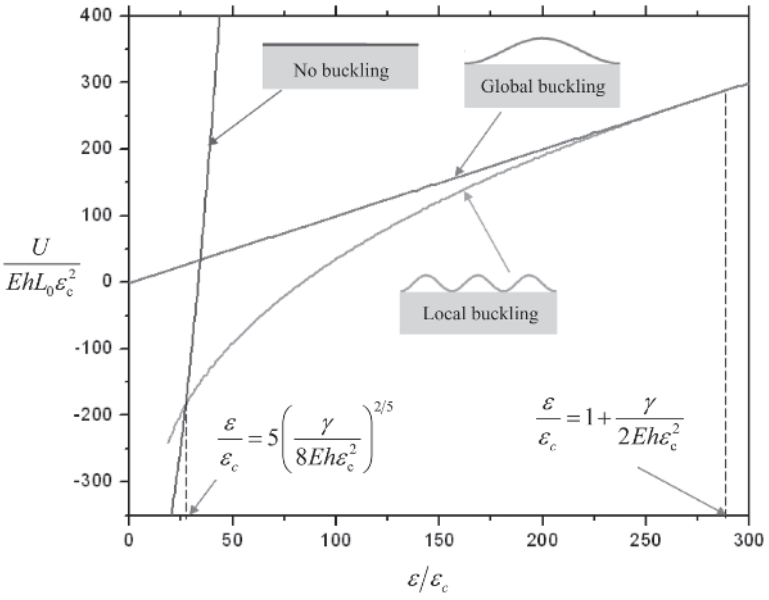

Figure 1.15 Comparison of the energy curves for the global, local, and no buckling modes. (Reprinted with permission from Ref. [39] Copyright 2010 The Royal Society of Chemistry).

occurs when $U_{\text{local}} = U_{\text{global}}$, which gives the critical strain for transition from local to global buckling as

$$\left(\frac{\varepsilon}{\varepsilon_c}\right)_{\text{local-global}} = 1+\frac{\gamma}{2Eh\varepsilon_c^2} \tag{1.47}$$

Figure 1.15 shows the normalized total energy for no buckling, local buckling, and global buckling versus the normalized compressive strain $\varepsilon/\varepsilon_c$. For the polyimide interconnect with $E = 2.5\,\text{GPa}$, $h = 1.4\,\mu\text{m}$, $L = 150\,\mu\text{m}$, and the work adhesion $\gamma = 0.16\,\text{J m}^{-2}$, $\frac{\gamma}{8Eh\varepsilon_c^2} = 70$, which predicts local buckling first and then global buckling as the compressive strain increases. For the strain smaller than 0.78% (Eq. (1.46)), the total energy for no buckling is the lowest. Local buckling prevails until the compressive strain reaches 8.0% from Eq. (1.47), at which global buckling has the lowest energy. The two strains 0.78% and 8.0% are consistent with the ranges of strains for no, local, and global buckling modes observed in Figure 1.14.

1.4.3
Large Deformation Effect on Buckling of Interconnects

In Sections 1.4.1 and 1.4.2, the buckling profile of the ribbon is assumed to be a sinusoidal form, which satisfying vanishing displacement and slope at the two ends. Those results are referred as small deformation model. However, when the compressive strain is large, the buckling profile will deviate from sinusoidal form, and the ends may rotate since the substrate is very compliant. Chen *et al.* [40] developed a mechanics model to describe the deformation of the buckled thin film by discarding the assumptions of sinusoidal form for the buckling profile and zero rotation at the two ends. The nonvanishing rotation at the ends is accounted by a rotational spring with a spring constant k.

Figure 1.16a shows the initial, strain-free configuration of the interconnect with a length L_0. The distance between two ends becomes L after buckling, and Figure 1.16b shows the deformed configuration and forces acting on the interconnect. The bending moment M_0 at the ends is related to the rotation θ_0 by $M_0 = k\theta_0$. The doubly clamped and simply supported boundary corresponds to the two limit cases $k \to \infty$ and $k \to 0$, respectively. The intrinsic coordinate (s,θ) as shown in Figure

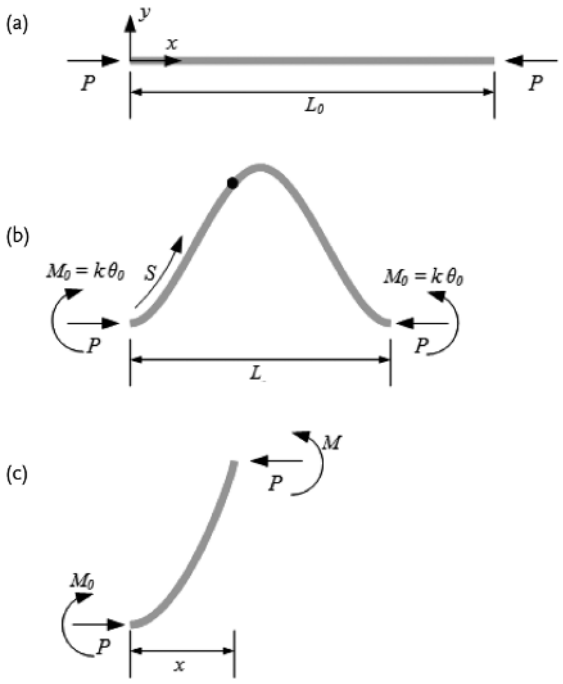

Figure 1.16 Schematic diagram of mechanics model for the thin film with torsional springs at the two ends. (Reprinted with permission from Ref. [3] Copyright 2011 The Chinese Society of Theoretical and Applied Mechanics).

1.16b is used to describe the deformation of the interconnects. Here s is the arc length from the left end to a point on the deformed shape and θ is the slope angle at that point. The coordinate (x, y) is related to (s,θ) by $dx/ds = \cos\theta$ and $dy/ds = \sin\theta$. The equilibrium equation of the beam is then given by

$$EI\frac{d\theta}{ds} = k\theta_0 - Py \tag{1.48}$$

where $EI = \bar{E}h^3/12$ is bending rigidity, and P is the compressive load at the ends. The boundary conditions are

$$\begin{aligned} &x(0) = 0, \quad x(L_0) = L_0 - u \\ &y(0) = 0, \quad y(L_0) = 0 \\ &\theta(0) = \theta_0, \quad \theta(L_0) = \pi - \theta_0 \end{aligned} \tag{1.49}$$

Equations (1.1) and (1.2) can be written in nondimensional form as

$$\frac{d\theta}{d\bar{s}} + \bar{P}y = \bar{k}\theta_0 \tag{1.50}$$

and

$$\begin{aligned} &\bar{x}(0) = 0, \quad \bar{x}(1) = 1 - \bar{u} \\ &\bar{y}(0) = 0, \quad \bar{y}(1) = 0 \\ &\theta(0) = \theta_0, \quad \theta(1) = \pi - \theta_0 \end{aligned} \tag{1.51}$$

where $\bar{x} = x/L_0$, $\bar{y} = y/L_0$, $\bar{s} = s/L_0$, $\bar{k} = kL_0/EI$, $\bar{P} = PL_0^2/EI$ and $\bar{u} = u/L_0$.

Equations (1.50) and (1.51) give

$$\frac{d\theta}{d\bar{s}} = \pm\sqrt{4\bar{P}C^2 - 4\bar{P}\sin^2\frac{\theta}{2}} \tag{1.52}$$

where C satisfies

$$4\bar{P}C^2 = \left(\bar{k}\theta_0\right)^2 + 4\bar{P}\sin^2\frac{\theta_0}{2} \tag{1.53}$$

The plus and minus sign distinguish between buckling to the top and to the bottom. Here, the minus sign is considered. Equation (1.52) then becomes

$$\frac{d\phi}{\sqrt{1 - C^2\sin^2\phi}} = -\sqrt{\bar{P}}d\bar{s} \tag{1.54}$$

where $\sin(\theta/2) = C\sin\varphi$. Integrating Eq. (1.54) from the end $(\bar{s} = 0, \varphi = \varphi_1)$ of the beam to the midlength $(\bar{s} = 0, \varphi = 0)$ gives

$$\int_{\varphi=0}^{\varphi=\varphi_1} \frac{d\varphi}{\sqrt{1 - C^2\sin^2\varphi}} = \frac{1}{2}\sqrt{\bar{P}} \tag{1.55}$$

where φ_1 satisfies

$$\sin(\theta_0/2) = C\sin\varphi_1 \tag{1.56}$$

Equations (1.53), (1.55), and (1.56) give the solutions of C, $\overline{P}$, and φ_1 for any given θ_0. The shortening $\overline{u}$ (i.e., compressive strain ε) and maximum deflection $\overline{y}_{\max}$ of the beam are then obtained as

$$\varepsilon = \overline{u} = 2 - \frac{4\int_{\varphi=0}^{\varphi=\varphi_1}\sqrt{1-C^2\sin^2\varphi}\,\mathrm{d}\varphi}{\sqrt{\overline{P}}} \tag{1.57}$$

and

$$\overline{y}_{\max} = \frac{2C}{\sqrt{\overline{P}}}(1-\cos\varphi_1) \tag{1.58}$$

Figure 1.17 shows normalized midspan deflection $\overline{y}_{\max}$ versus the compressive strain ε with different normalized torsional spring constant $\overline{k}$. The dotted line is from the previous small deformation model in Section 1.4.1 and the solid lines from Eqs. (1.57) and (1.58). The finite element results are also given for comparison. The current results (solid line) agree well with finite element simulations, while previous small deformation model overestimates the deflection as the compressive strain increases. It should be noted that $\overline{y}_{\max}$ is almost same for doubly clamped ($\overline{k} = 1000$) and simply supported ends ($\overline{k} = 0$), while $\overline{y}_{\max}$ becomes slightly larger for midvalue $\overline{k}$. For example, $\overline{y}_{\max}$ for $\overline{k} = 40$ is 3% larger than that for $\overline{k} = 0$ at $\varepsilon = 50\%$.

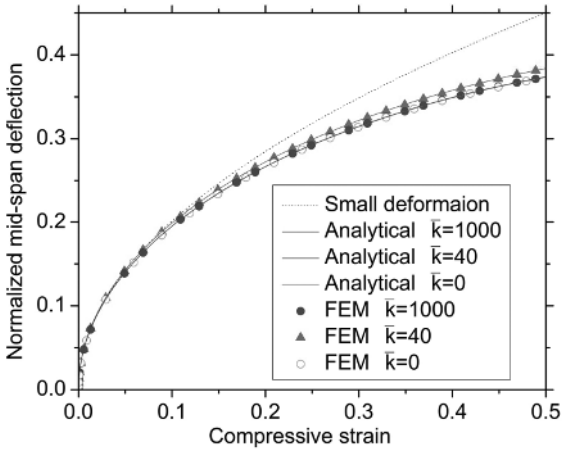

Figure 1.17 The normalized midspan deflection $\overline{y}_{\max}$ versus the compressive strain ε with different normalized torsional spring constant $\overline{k}$. (Reprinted with permission from Ref. [3] Copyright 2011 The Chinese Society of Theoretical and Applied Mechanics).

1.5 Concluding Remarks

We have reviewed the mechanics of the stretchable wavy ribbon, popup structure, and interconnects in the noncoplanar mesh design. Both the buckling geometry (wavelength and amplitude) and the maximum strains are obtained analytically. The solutions agree well with the experiments and finite element simulations and clearly show how wavy profile reduces the strain to achieve large stretchability.

Stretchable wavy ribbons: In this case, the ribbon is chemically bonded to the substrate and no delamination occurs. Both small-deformation and finite-deformation analysis are performed for this system. The finite-deformation model predicts a strain-dependent wavelength, while the small-deformation one gives a strain-independent wavelength. The finite width effects have been studied analytically. The experimental and analytical results show that both the buckling amplitude and wavelength increase with the film width.

Popup structure: In this case, the ribbon is only bonded to the substrate at certain locations. When the prestrain is released, the portion of the ribbon without bonding to the substrate delaminates from the substrate and forms the popup structure. The wavelength and amplitude only depend on the geometry and can be precisely controlled to lower the maximum strain to have larger stretchability.

Interconnects in the noncoplanar mesh designs: In this case, the popup interconnects, which is loosely bonded to the substrate, are used to link the device islands, which are chemically bonded to the substrate. The adhesion between the interconnects and substrate is accounted to explain different buckling patterns. The large deformation effect on the buckling of the interconnects is also considered.

References

1 Crawford, G.P. (2005) *Flexible Flat Panel Display Technology*, John Wiley & Sons, Inc., New York.

2 Jin, H.C., Abelson, J.R., Erhardt, M.K., and Nuzzo, R.G. (2004) Soft lithographic fabrication of an image sensor array on a curved substrate. *J. Vac. Sci. Technol. B*, **22**, 2548–2551.

3 Ko, H.C., Stoykovich, M.P., Song, J., Malyarchuk, V., Choi, W.M., Yu, C.J., Geddes, J.B., Xiao, J., Wang, S., Huang, Y., and Rogers, J.A. (2008) A hemispherical electronic eye camera based on compressible silicon optoelectronics. *Nature*, **454**, 748.

4 Shin, G., Jung, I., Malyarchuk, V., Song, J., Wang, S., Ko, H.C., Huang, Y., Ha, J.S., and Rogers, J.A. (2010) Micromechanics and advanced designs for curved photodetector arrays in hemispherical electronic eye cameras. *Small*, **6**, 851–856.

5 Lumelsky, V.J., Shur, M.S., and Wagner, S. (2001) Sensitive skin. *IEEE Sens. J.*, **1**, 41–51.

6 Someya, T., Sekitani, T., Iba, S., Kato, Y., Kawaguchi, H., and Sakurai, T. (2004) A large-area, flexible pressure sensor matrix with organic field-effect transistors for artificial skin applications.

Proc. Natl. Acad. Sci. USA, **101**, 9966–9970.

7 Nathan, A., Park, B., Sazonov, A., Tao, S., Chan, I., Servati, P., Karim, K., Charania, T., Striakhilev, D., Ma, Q., and Murthy, R.V.R. (2000) Amorphous silicon detector and thin film transistor technology for large-area imaging of X-rays. *Microelectron. J.*, **31**, 883–891.

8 Garnier, F., Hajlaoui, R., Yassar, A., and Srivastava, P. (1994) All-polymer field-effect transistor realized by printing techniques. *Science*, **265**, 1684–1686.

9 Baldo, M.A., Thompson, M.E., and Forrest, S.R. (2000) High-efficiency fluorescent organic light-emitting devices using a phosphorescent sensitizer. *Nature*, **403**, 750–753.

10 Crone, B., Dodabalapur, A., Lin, Y.Y., Filas, R.W., Bao, Z., LaDuca, A., Sarpeshkar, R., Katz, H.E., and Li, W. (2000) Large-scale complementary integrated circuits based on organic transistors. *Nature*, **403**, 521–523.

11 Loo, Y.L., Someya, T., Baldwin, K.W., Bao, Z., Ho, P., Dodabalapur, A., Katz, H., and Rogers, J.A. (2002) Soft, conformable electrical contacts for organic semiconductors: high-resolution plastic circuits by lamination. *Proc. Natl. Acad. Sci. USA*, **99**, 10252–10256.

12 Facchetti, A., Yoon, M.H., and Marks, T.J. (2005) Gate dielectrics for organic field-effect transistors: new opportunities for organic electronics. *Adv. Mater.*, **17**, 1705–1725.

13 Sekitani, T., Noguchi, Y., Hata, K., Fukushima, T., Aida, T., and Someya, T. (2008) A rubberlike stretchable active matrix using elastic conductors. *Science*, **321**, 1468–1472.

14 Gray, D.S., Tien, J., and Chen, C.S. (2004) High-conductivity elastomeric electronics. *Adv. Mater.*, **16**, 393–397.

15 Hung, P.J., Jeong, K., Liu, G.L., and Lee, L.P. (2004) Microfabricated suspensions for electrical connections on the tunable elastomer membrane. *Appl. Phys. Lett.*, **85**, 6051–6053.

16 Lacour, S.P., Jones, J., Wanger, S., Li, T., and Suo, Z. (2005) Stretchable interconnects for elastic electronic surfaces. *Proc. IEEE*, **93**, 1459–1467.

17 Khang, D.Y., Jiang, H.Q., Huang, Y., and Rogers, J.A. (2006) A stretchable form of single-crystal silicon for high-performance electronics on rubber substrate. *Science*, **311**, 208–212.

18 Kim, D.H., Ahn, J.H., Choi, W.M., Kim, H.S., Kim, T.H., Song, J., Huang, Y., Liu, Z.J., Lu, C., and Rogers, J.A. (2008) Stretchable and foldable silicon integrated circuits. *Science*, **320**, 507–511.

19 Kim, D.H., Song, J., Choi, W.M., Kim, H.S., Kim, R.H., Liu, Z., Huang, Y., Hwang, K.C., Zhang, Y., and Rogers, J.A. (2008) Materials and non-coplanar mesh designs for integrated circuits with linear elastic responses to extreme mechanical deformations. *Proc. Natl. Acad. Sci. USA*, **105**, 18675–18680.

20 Kim, D.H., Choi, W.M., Ahn, J.H., Kim, H.S., Song, J., Huang, Y., Liu, Z.J., Lu, C., Koh, C., and Rogers, J.A. (2008) Complementary metal oxide silicon integrated circuits incorporating monolithically integrated stretchable wavy interconnects. *Appl. Phys. Lett.*, **93**, 044102.

21 Hsu, Y.Y., Gonzalez, M., Bossuyt, F., Axisa, F., Vanfleteren, J., and Wolf, I.D. (2011) The effects of encapsulation on deformation behavior and failure mechanism of stretchable interconnects. *Thin Solid Films*, **519**, 2225–2234.

22 Kim, D.H., Liu, Z., Kim, Y.S., Wu, J., Song, J., Kim, H.S., Huang, Y., Hwang, K.C., Zhang, Y., and Rogers, J.A. (2009) Optimized structural designs for stretchable silicon integrated circuits. *Small*, **5**, 2841–2847.

23 Jiang, H., Sun, Y., Rogers, J.A., and Huang, Y. (2007) Mechanics of precisely controlled thin film buckling on elastomeric substrate. *Appl. Phys. Lett.*, **90**, 133119.

24 Bowden, N., Brittain, S., Evans, A.G., Hutchinson, J.W., and Whitesides, G.M. (1998) Spontaneous formation ordered structures in thin films of metals supported on an elastomeric polymer. *Nature*, **393**, 146–149.

25 Choi, W.M., Song, J., Khang, D.Y., Jiang, H., Huang, Y., and Rogers, J.A. (2007) Biaxially stretchable "wavy" silicon nanomembranes. *Nano Lett.*, **7**, 1655–1663.

26 Sun, Y., Choi, W.M., Jiang, H., Huang, Y., and Rogers, J.A. (2006) Controlled buckling of semiconductor nano ribbons for stretchable electronics. *Nat. Nanotechnol.*, **1**, 201–207.

27 Jiang, H., Khang, D.Y., Fei, H., Kim, H., Huang, Y., Xiao, J., and Rogers, J.A. (2008) Finite width effect of thin-films buckling on compliant substrate: experimental and theoretical studies. *J. Mech. Phys. Solids*, **56**, 2585–2598.

28 Chen, X., and Hutchinson, J.W. (2004) Herringbone buckling patterns of compressed thin films on complaint substrates. *J. Appl. Mech.-Trans. ASME*, **71**, 597–603.

29 Huang, Z.Y., Hong, W., and Suo, Z. (2005) Nonlinear analyses of wrinkles in a film bonded to a compliant substrate. *J. Mech. Phys. Solids*, **53**, 2101–2118.

30 Stafford, C.M., Harrison, C., Beers, K.L., Karim, A., Amis, E.J., Vanlandingham, M.R., Kim, H.C., Volksen, W., Miller, R.D., and Simonyi, E.E. (2004) A buckling-based metrology for measure the elastic moduli of polymeric thin films. *Nat. Mater.*, **3**, 545–550.

31 Stafford, C.M., Vogt, B.D., Harrison, C., Julthongpiput, D., and Huang, R. (2006) Elastic moduli of ultrathin amorphous polymer films. *Macromolecules*, **39**, 5095–5099.

32 Volynskii, A.L., Bazhenov, S., Lebedeva, O.V., and Bakeev, N.F. (2000) Mechanical buckling instability of thin coatings deposited on soft polymer substrates. *J. Mater. Sci.*, **35**, 547–554.

33 Harrison, C., Stafford, C.M., Zhang, W.H., and Karim, A. (2004) Sinusoidal phase grating created by tunably buckled surface. *Appl. Phys. Lett.*, **85**, 4016–4018.

34 Jiang, H., Khang, D.Y., Song, J., Sun, Y., Huang, Y., and Rogers, J.A. (2007) Finite deformation mechanics in buckled thin films on compliant supports. *Proc. Natl. Acad. Sci. USA*, **104**, 15607–15612.

35 Song, J., Jiang, H., Liu, Z., Khang, D.Y., Huang, Y., Rogers, J.A., Lu, C., and Koh, C.G. (2008) Buckling of a stiff thin film on a compliant substrate in large deformation. *Int. J. Solids Struct.*, **45**, 3107–3121.

36 Song, J., Huang, Y., Xiao, J., Wang, S., Hwang, K.C., Ko, H.C., Kim, D.H., Stoykovich, M.P., and Rogers, J.A. (2009) Mechanics of non-coplanar mesh design for stretchable electronic circuits. *J. Appl. Phys.*, **105**, 123516.

37 Ko, H.C., Shin, G., Wang, S., Stoykovich, M.P., Lee, J.W., Kim, D.H., Ha, J.S., Huang, Y., Hwang, K.C., and Rogers, J.A. (2009) Curvilinear electronics formed using silicon membrane circuits and elastomeric transfer elements. *Small*, **5**, 2703–2709.

38 Wang, S., Xiao, J., Song, J., Ko, C.H., Hwang, K.C., Huang, Y., and Rogers, J.A. (2010) Mechanics of curvilinear electronics. *Soft Matter*, **6**, 5757–5763.

39 Song, J., Jiang, H., Huang, Y., and Rogers, J.A. (2009) Mechanics of stretchable inorganic electronic materials. *J. Vac. Sci. Technol. A*, **27**, 1107–1125.

40 Chen, C., Tao, W., Liu, Z.J., Zhang, Y.W., and Song, J. (2011) Controlled buckling of thin film on elastomeric substrate in large deformation. *Theor. Appl. Mech. Lett.*, **2**, 021001.